Application of a Reynolds-Averaged Navier-Stokes Approach to Supersonic Retropropulsion Flowfields

Ashley M. Korzun,* Ian G. Clark,† and Robert D. Braun‡
Georgia Institute of Technology, Atlanta, Georgia, 30332, USA

Systems analysis efforts have identified supersonic retropropulsion as a candidate decelerator technology for the human exploration of the surface of Mars. These efforts are presently challenged by a lack of available models and are looking to computational fluid dynamics analyses for databases representing the aerodynamic-propulsive interactions inherent to supersonic retropropulsion. This work uses a Reynolds-averaged Navier-Stokes approach to predict the flowfield structure, surface pressure distributions, and integrated aerodynamic force coefficients for four configurations recently tested in the NASA Langley Research Center Unitary Plan Wind Tunnel. These configurations have zero, one, three, and four nozzles on the model forebody. Comparisons are made with experimental data for static pressure distributions on the forebody and aftbody, and computational schlieren images illustrating the resulting flowfields have also been generated. The results of this work illustrate the applicability of the Reynolds-averaged Navier Stokes equations to this problem through comparison with data from a test series designed explicitly for the validation of computational fluid dynamics tools in simulating supersonic retropropulsion flowfields. The Reynolds-averaged Navier-Stokes approach applied performed well in predicting the surface pressure distribution and flowfield structure for supersonic retropropulsion configurations with single and multiple nozzles at zero degrees angle of attack and a thrust coefficient of approximately 2.0.

Nomenclature

A	Area, m^2
C	Coefficient
d	Diameter, m
M	Mach number
N	Number of grid nodes
p	Pressure, lb/in^2
q	Dynamic pressure, N/m^2
r	Radius, m
T	Temperature, K
t	Time, s
$\dot{m}$	Mass flow rate, lb_m/s
x	Axial location, m
α	Angle of attack, deg
γ	Ratio of specific heats
τ	Thrust, N
ϕ	Angular location, deg

Subscripts and Superscripts

A	Axial
a	Ambient condition
D	Drag
e	Nozzle exit condition
f	Forebody
j	Jet Condition
L	Lift
M	Pitching moment
m	Model
ref	Reference condition
p	Pressure
T	Thrust
∞	Freestream condition
0	Total condition
$*$	Nozzle throat condition

*Graduate Research Assistant, Daniel Guggenheim School of Aerospace Engineering, AIAA Student Member.
†Visiting Assistant Professor, Daniel Guggenheim School of Aerospace Engineering, AIAA Member.
‡David and Andrew Lewis Associate Professor of Space Technology, Daniel Guggenheim School of Aerospace Engineering, AIAA Fellow.

I. Introduction

To achieve NASA's long-term exploration goals at Mars, namely human exploration of the surface, technologies are needed that enable more than an order of magnitude increase in landed mass (10s of metric tons), four orders of magnitude increase in landing accuracy (meters), and landings at higher surface elevations (0+ km).[1,2] Supersonic deceleration has been identified as a critical deficiency in extending existing technologies to high mass, high ballistic coefficient systems. As the development and qualification of significantly larger supersonic parachutes is not a viable path forward for increasing landed mass capability to 10+ metric tons, alternative deceleration approaches must be developed.[1]

NASA has expended significant effort to identify enabling technologies to support human exploration at Mars. As a part of this effort, eight candidate entry, descent, and landing (EDL) architectures have been developed.[2] Four of these eight architectures rely on the initiation of a retropropulsion phase at supersonic conditions, or supersonic retropropulsion (SRP). The evaluation of SRP concepts and comparison of these concepts with alternative decelerators is currently challenged by a lack of SRP aerodynamic models. Given the limitations of existing experimental data[3] and the inability to fully simulate Mars-relevant conditions and configurations in ground-based facilities, the development of these models will likely depend heavily on the use of validated computational fluid dynamics (CFD) tools. The validation of existing CFD approaches and tools is currently underway.[4,5]

Prior work by the authors focused on describing the relevant flow physics of supersonic retropropulsion and exploratory investigation of historical test cases.[6] This investigation extends the Reynolds-averaged Navier-Stokes (RANS) CFD approach applied previously to CFD validation efforts for supersonic retropropulsion. The configurations and conditions used here are from a recent wind tunnel test designed explicitly to provide data for this purpose.[7] This work is intended to compliment on-going efforts to validate existing CFD tools for use in developing SRP aerodynamic databases for systems analysis.[4]

This paper is organized as follows. Section II describes supersonic retropropulsion flowfields and briefly reviews past work, emphasizing recent computational efforts for SRP problems. Section III describes the wind tunnel test and data used in this investigation. Section IV describes the computational tool, associated models, and cases and conditions of interest. Section V presents the results of a grid refinement study. Lastly, Section VI presents and discusses the results and comparisons with experimental data for each of the four configurations examined.

II. Background

Exploratory development efforts from the 1960s and early 1970s still form much of the current knowledge base for supersonic retropropulsion. A significant number of wind tunnel experiments with sub-scale models were completed during this time. These were mostly exploratory and disjoint investigations for EDL applications, with prototypical Mars landers in mind by the late 1960s. This work is almost exclusively on SRP configurations with a single nozzle at the nose of a blunt vehicle geometry. Development efforts ceased with the selection of supersonic parachutes for the Viking landers in the early 1970s, and only recently has interest in SRP resurfaced. Additional detail on past work is given in a recent review of the SRP literature by Korzun et al.[3]

A. Supersonic Retropropulsion Flowfields

The supersonic retropropulsion flowfield is a complex interaction between a typically highly under-expanded jet and the shock layer of a body in supersonic flow. Figure 1 (adapted[3,8]) illustrates the general features of the resulting flowfield. The flow features in Fig. 1 are briefly discussed in this section; see Ref. 6 for additional detail. Flowfields surrounding blunt bodies with no retropropulsion, configurations with jet flow from a single nozzle at the center of the vehicle forebody, and configurations with multiple nozzles on the vehicle forebody each exhibit unique behaviors. The three SRP configurations explored in this work are expected to yield flowfields spanning this set of behaviors.

In general, highly under-expanded jet flows (p_e is sufficiently greater than p_a) exhausting from a body into a quiescent medium are characterized by an expansion fan bounded by a barrel shock and termination of the jet with a Mach disk.[9–11] From the nozzle exit, the jet flow undergoes Prandtl-Meyer expansion until the jet pressure equals the local ambient pressure, defining the high-velocity jet boundary.[9] At highly

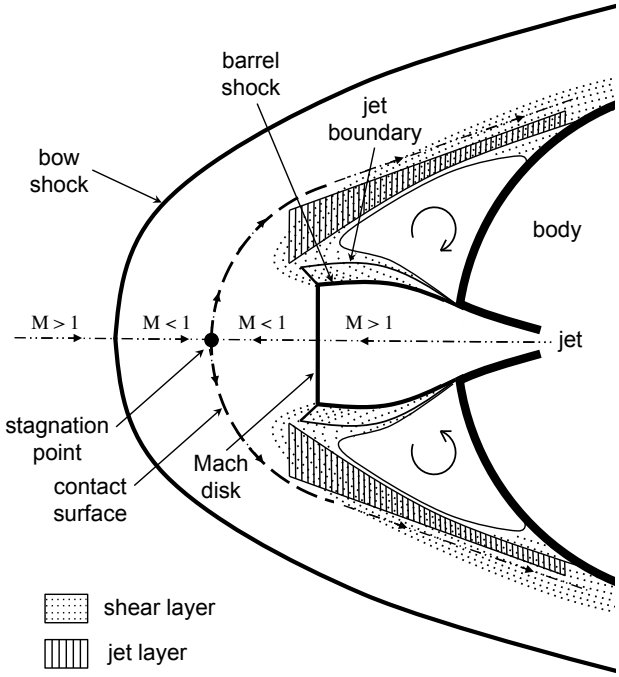

Figure 1. Illustration of primary flow features for simple SRP flowfields (Adapted[6,8]).

under-expanded conditions, a Mach disk forms as a part of a shock intersection away from the jet centerline, and characteristic lines coalesce to form a barrel shock between the jet core and the jet boundary.

At the triple point, or the intersection of the Mach disk and the barrel shock, an oblique reflected shock forms. This intersecting structure is thought to arise from the formation of a sonic, throat-like region allowing the subsonic jet core downstream of the Mach disk to be supersonic on the side of the Mach disk nearer the nozzle exit.[12] For jet flows exhausting exclusively into static, quiescent mediums, this theory is analogous to the Mach disk forming where a normal shock has sufficient strength to equate the static pressure behind the shock to the local ambient pressure.[12]

A bow shock forms upstream of the body as a result of the jet structure obstructing the oncoming freestream. The supersonic freestream flow is decelerated to subsonic conditions in the stagnation region by the bow shock, and the supersonic jet flow is decelerated to subsonic conditions by the jet termination structure, typically a Mach disk. Observations in the literature, however, and also in the high-speed schlieren video from the test of interest in this investigation, point out that even in the most steady flowfields, the jet termination structure often oscillates between a Mach disk and a lambda shock. The stagnation region is bounded by two supersonic regions (the freestream and jet flows) and consists of a subsonic region divided by a contact discontinuity at the intersection of the two flows.[8] This contact surface separates the subsonic jet core and the subsonic flow behind the bow shock. The contact surface is the freestream flow obstruction for SRP flowfields.

The freestream flow being swept downstream and the supersonic and subsonic flow within the shear layer are drawn toward the regions of lower pressure near the jet, contributing to the formation of recirculation regions over the forebody for configurations with centrally-located nozzles. The shear layer is the parallel-velocity mixing region in the shock layer along the barrel shock and the jet boundary. This mixing region has been found to significantly impact the diffusion of the jet flow away from the nozzle exit.[8,12] The large velocity gradients between the subsonic flow behind the bow shock and the opposing supersonic jet flow form the supersonic shear layer along the outer jet boundary. The recirculation and high pressure behind the bow shock force significant mixing within the shear layer as the jet flow is turned outboard. The overall effect of the jet-shock layer interaction is the shielding of the body from the freestream, resulting in the body being blanketed by an annular region of relatively constant pressure on the downstream side of the contact surface.

The degree of formation of the primary flow features and the stability (and also steadiness) of the flowfield are highly dependent on the retropropulsion configuration and the relative strength of the jet flow, of-

ten given as a function of the ratio of the total pressure of the jet flow to the total pressure of the freestream. The exit Mach number of the nozzle, M_e, and composition of the jet flow, γ_j, also influence flowfield structure.[8] For a fixed set of freestream conditions, thrust coefficient, C_T (defined in Eq. (1)), is often used as a similarity parameter to gauge the strength of the jet flow relative to the freestream. As a force coefficient, C_T is the most common parameter used in the literature to characterize the change in the vehicle's aerodynamic characteristics resulting from SRP. Equation 1, assuming an ideal, calorically perfect gas, isentropic flow, and neglecting the ambient pressure contribution to thrust, gives the relationship between thrust coefficient and the ratio of the jet total pressure to the freestream total pressure. System-level performance analyses have determined flight-relevant operating conditions for SRP to be $M_\infty < 3.0$ and $C_T > 8.0$ for human-scale missions.[2,13]

$$\begin{aligned} C_T &= \frac{\tau}{q_\infty A_{ref}} \\ &= \frac{2(1+\gamma_e M_e^2)}{\gamma_\infty M_\infty^2} \cdot \frac{A_e}{A_{ref}} \cdot \left(1+\frac{\gamma_e-1}{2}M_e^2\right)^{-\frac{\gamma_e}{\gamma_e-1}} \cdot \left(1+\frac{\gamma_\infty-1}{2}M_\infty^2\right)^{\frac{\gamma_\infty}{\gamma_\infty-1}} \cdot \frac{p_{0,j}}{p_{0,\infty}} \end{aligned} \tag{1}$$

B. Prior Computational Fluid Dynamics Analyses

In general, accurate prediction of the static aerodynamics and flowfield behaviors for supersonic retropropulsion using CFD methods likely requires the ability to capture:

- Detached shocks
- Highly under-expanded jet flow structures
- Contact surfaces
- Formation and turbulent transition of free shear layers
- Local and global unsteadiness within the flowfield

Inviscid, laminar, and turbulent CFD analyses have been applied to SRP-like flow problems, with varying degrees of success. The similarities between the flow interactions across these works has been useful in extending the approaches to analyses targeting SRP applications. As such, a number of more recent analyses are reviewed here, focusing on the analyses of configurations and conditions tested by Daso et al.[14] and Jarvinen and Adams.[15]

Inviscid computational approaches have shown reasonable success in capturing the locations of primary flow features, surface pressure distributions, and integrated force coefficients over the limited range of conditions and configurations considered. Bakhtian et al.[16] conducted a parametric investigation into SRP configurations using Cart3D, a Cartesian-based Euler solver with adjoint-based mesh refinement for steady-state solutions. The configurations and conditions explored were derived from those used by Jarvinen and Adams[15] (60-deg sphere-cone aeroshell, M_∞ = 2.0, M_e = 4.3, central and peripheral nozzle locations on the forebody, and C_T = 0 to 7). All flow solutions were steady-state. The results followed similar trends to those observed in the original experiment for $C_{A,total}$ as a function of C_T, though the comparison became less agreeable at higher thrust coefficients for the multiple nozzle configuration. A reduction in surface pressures was achieved for the multiple nozzle configuration but at higher thrust coefficients than observed in the original experiment, suggesting some difficulty simulating the inboard jet flow expansion and interaction of jet boundaries with one another. No flowfield images were given for the cases compared with experimental data, but an apparent reduction of grid resolution in the bow shock region, despite adjoint-based mesh refinement, may have contributed to the difficulties capturing the inboard flowfield structure. In general though, the computational results agree reasonably well with the locations of primary flow features and trends in surface pressure distributions and integrated force coefficients reported in the original experiment, supporting the predominance of inviscid flow phenomena in SRP flowfields.

Daso et al.,[14] Chang et al.,[17] and Cheng et al.[18] conducted analyses using a 2.6%-scale Apollo capsule with and without retropropulsion effects. In all cases, the analyses were attempting to predict the aerodynamic and aerothermal effects of a centrally-located nozzle exhausting air (into air) at freestream Mach

numbers of 3.48 and 4.0. As the pressure data from the experiment were not sufficient for quantitative comparison, each analysis focused on matching experimental heat flux values. Daso et al.,[14] conducting RANS simulations with a pointwise Goldberg one-equation turbulence model, predicted peak heat fluxes with unsteadiness that were significantly higher than the baseline heat flux, though the overall trends were consistent with the experiment and other cases in the literature. Chang et al.[17] used both laminar and turbulent ($k-\epsilon$ turbulence model) approaches to obtain time-accurate solutions. The results noted significant unsteadiness for all cases with jet flow, and the time histories for drag force and heat flux exhibited low frequency, large amplitude oscillations. Depending on the mass flow rate of the jet, the results either over-predicted or under-predicted surface heat flux. Cheng et al.[18] extended this work to include a finite-rate chemistry model for air, though no reactions were observed at the relatively low temperature conditions in the experiment (T_0 = 300 K). In comparing with experimental data, the computational results over-predicted heat flux, qualitatively under-predicted surface pressures, and did not capture the flow mode transition at the exact conditions reported in the experiment. The work cited a possible explanation for pressure discrepancies as the tendency of two-equation turbulence models (a $k-\epsilon$ model was applied in the analysis) to over-predict the jet spreading rate due to compressibility effects, resulting in a smaller, but stronger recirculation zone near the surface. There was qualitatively good agreement with schlieren images in all three sets of analyses.

NASA's Exploration Technology Development and Demonstration Program includes efforts to assess the capabilities of existing computational tools in simulating SRP flowfields. Recent work[6,19,20] applied three NASA-developed CFD codes to experimental work completed by Daso et al.[14] and Jarvinen and Adams[15] and to planning for the wind tunnel test described in Section III.[7] FUN3D (with Menter's shear stress transport (SST) turbulence model), OVERFLOW (with a strain-based SST turbulence model), and DPLR (with Menter's SST turbulence model) were the three codes applied. For the single, central nozzle configuration from Jarvinen and Adams,[15] all three codes over-predicted the location of primary flow features (bow shock, free stagnation point, Mach disk), with FUN3D and OVERFLOW results showing a pressure rise at the shoulder that was inconsistent with the experimental data. For the three nozzle, peripheral configuration from Jarvinen and Adams,[15] FUN3D and OVERFLOW predicted much higher pressures at the nose than were reported in the original experiment for conditions of C_T = 4.04 and C_T = 7.0. Both qualitative and quantitative comparisons were reasonably good for C_T = 1.00 conditions. All three codes showed good qualitative agreement with experimental schlieren for the case taken from Daso et al.[14] In general, grid resolution was found to be extremely important, with under-resolving the barrel shock and shear layer regions often leading to a jet termination structure with a different Mach reflection and under-resolving the region for the jet termination shock often resulting in a completely different jet boundary shape than that expected with no jet termination structure.

Completion of more focused computational simulations of the interactions between highly under-expanded retropropulsion exhaust flows and shock layers at supersonic conditions is the next step required to continue maturing supersonic retropropulsion from a potentially feasible concept to a viable alternative for advanced EDL architectures. Much of the physics relevant to SRP flowfield behavior is highly coupled, with the modeling of viscosity and turbulence being important factors in accurately predicting flowfield structure and pressure distributions. However, inviscid approaches have demonstrated, at least for limited conditions and configurations, that SRP flow phenomena are predominantly inviscid in nature, and this may be significant in reducing the computational effort required to generate the much needed SRP models for systems analysis applications. Flow separation, recirculation, boundary layer transition, and oscillation of the primary flow features, such as the bow shock, stagnation region, contact surface, barrel shock, jet flow boundary, and reflected jet termination structures, are relevant characteristics of supersonic retropropulsion flowfields. Computational solutions that accurately capture these characteristics exist under a very limited range of conditions at this point.

III. Experiment Summary and Available Data Set

The experimental data used in this investigation are from a supersonic retropropulsion test completed under NASA's Exploration Technology Development and Demonstration Program in the NASA Langley Research Center (LaRC) 4 ft. $\times$ 4 ft. Unitary Plan Wind Tunnel (UPWT) in July 2010.[7] This test was explicitly designed to provide experimental data for concurrent CFD validation efforts and uncertainty analyses. Additionally, it was the first test in nearly 40 years targeting flight-relevant conditions and applications of SRP

and represents a significant step forward in addressing the limitations of existing historical data sets.[3] Only a brief overview of the model, instrumentation, test data, and test conditions is given here; publications dedicated to the design of the test[5,7] and post-test data analysis[4,21] are available in the references.

The model, shown in Fig. 2, was a 5 inch-diam, 70-deg sphere-cone forebody with a 10 inch-long cylindrical aft housing. Four configurations were tested: zero nozzles, one central nozzle, three nozzles spaced 120° apart at the forebody half-radius, and four nozzles from the combination of the one and three nozzle configurations. Figure 2 also shows the three nozzle configuration of the model installed in the wind tunnel test section. The nozzles were conical, with an exit diameter, d_e, of 0.5 inch and an expansion ratio, A_e/A^*, of 4 (M_e = 2.94). The nozzles were axially-aligned; the three nozzles at the forebody half-radius were scarfed to have the exit plane of the nozzle flush with the model forebody. The composition of both the freestream and the nozzle flow was air.

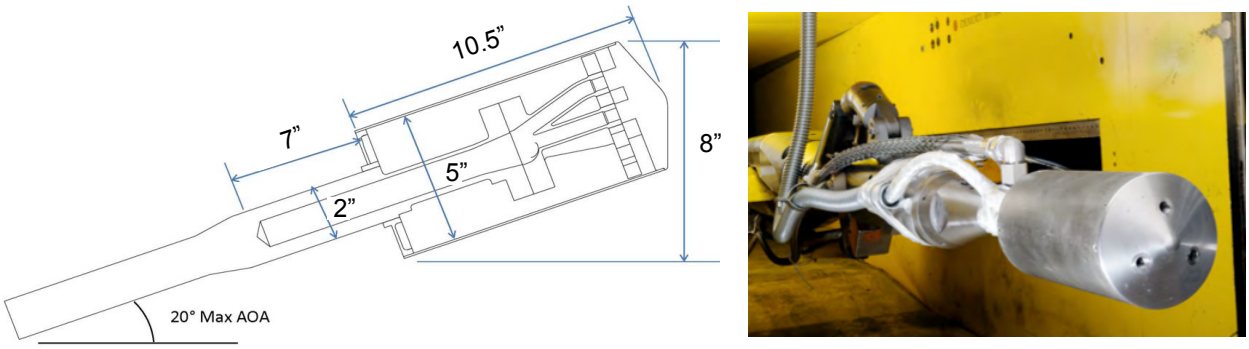

Figure 2. Model dimensions and the model installed in the wind tunnel test section.[7]

The model was instrumented with static pressure taps on the forebody and aft housing, Kulite pressure transducers (40 kHz) on the forebody for both time-averaged and unsteady pressure measurements, and internal pressure and temperature sensors. The static pressure measurements were taken at a 10 Hz sampling rate over a 2.5 sec test point interval. Figure 3 shows the pressure port layout on the model. The ports that have been filled in are the ports to be compared with CFD results in Section VI. There were 167 total surface pressure ports: 104 ports on the forebody, 49 ports on the aft housing, and 14 additional ports between three of the four nozzle plugs. Additionally, high-speed schlieren video was taken at frame rates up to 10,000 frames per second during the test. Examples of still images taken from the high-speed schlieren video for each of the four runs of interest in this investigation are given in the Appendix.

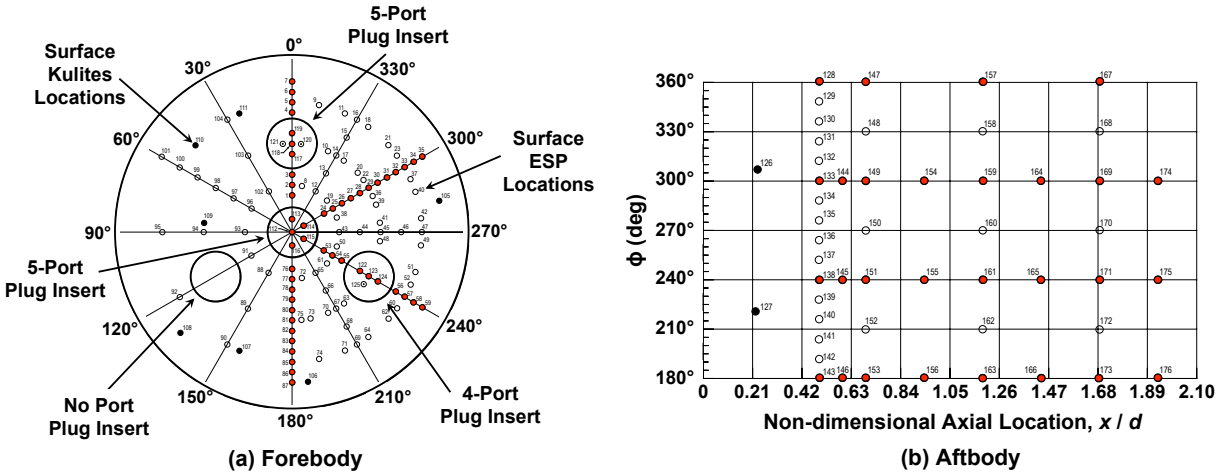

Figure 3. Pressure port locations and nozzle configurations. Ports of interest are filled.

Test conditions spanned three freestream Mach numbers (M_∞ = 2.4, 3.5, 4.6) and thrust coefficients up to 3.0 for each configuration. Thrust coefficients up to 6.0 were explored where possible, depending on the

nozzle configuration and degree of interference with the tunnel walls. The model was rolled through 180° (in 60° increments) and pitched through an angle of attack sweep from -8° to +20°, also depending on the nozzle configuration and degree of interference with the tunnel walls. The run matrix was defined to allow for quantification of various sources of experimental uncertainty, including random and bias errors.[7,21] Detailed data and uncertainty analysis is on-going; all comparisons in this paper have been made with raw test data. The following section discusses the specific runs and conditions to be used in this investigation.

IV. Models and Approach

This work uses a Reynolds-averaged Navier-Stokes approach to predict the flowfield structure, surface pressure distributions, and integrated aerodynamic force coefficients for the four configurations recently tested in the NASA Langley Research Center Unitary Plan Wind Tunnel.[7] Comparisons have been made with experimental data for static pressure on both the forebody and the aftbody of the model. A grid refinement study has also been completed and is discussed in Section V.

A. Computational Approach

FUN3D was the computational tool used for all CFD analyses completed in this investigation and was chosen for its past and current application to SRP flowfields.[4,6,19,20] FUN3D is a fully unstructured, NASA-developed CFD code capable of solving the Euler and RANS equations through both perfect gas and thermochemical equilibrium/non-equilibrium simulation.[22–24] The flow solver is based on second-order, node-centered, finite-volume discretization. Local time stepping is applied for steady flows, and second-order time accuracy is applied for unsteady flows. The scheme utilizes implicit upwind-differencing and, similar to recent work,[4,19,20] Edwards' dissipative LDFSS flux function[25] with a Van Albada limiter.[26] The RANS flow solver is loosely coupled to Menter's SST turbulence model,[27] with no compressibility correction. All of the "jet-on" cases were run using a time-accurate approach. All solutions were generated using version 11.4 of the FUN3D code.

Generation of the unstructured, tetrahedral grids used in this study was completed through a multi-step approach using GridEx / BatchEx[28] and VGRID / PostGRID.[29] Nodal, linear, and volume VGRID sources were defined to control the characteristics of the resulting grids. Increased resolution in the vicinity of the model surface was specified at the nozzle exit, nozzle throat, converging section of the nozzle, model shoulder, and aft end of the model. A conical volume source was applied to increase grid density in the jet flow interaction region upstream of the model. Additionally, a cylindrical volume source spanning the length of the computational domain was specified with a spacing gradient to assist with the convergence of the advancing front algorithm used by VGRID in generating the volume grid. The final grid spacing specifications were determined from a grid resolution study, described in Section V.

Iterative convergence was determined previously[6] through a three order of magnitude drop in the residuals of conservative quantities and maintenance of this drop through several hundred additional iterations. This work similarly determined iterative convergence through tracking residuals with iteration (mass, momentum, energy, turbulence) and terminating after the residuals reached and maintained a plateau or periodic oscillations for several hundred iterations.

As mentioned, a spatial convergence, or grid refinement, study was also completed. FUN3D does not currently include adjoint-based mesh refinement capability for use with Menter's SST turbulence model, and no direct quantities reflecting spatial discretization errors are available. As such, an alternative approach was recommended that uses a sequence of grids and shows the sensitivity of important dependent variables as the grid resolution becomes increasingly more fine.[30] The quantities tracked were the integrated drag and integrated lift of the forebody. The results of this study are given in Section V.

Unsteady solutions were computed using the BDF2OPT[31] scheme, theoretically second-order accurate. To assess temporal accuracy, a temporal error controller was employed to run subiterations until the subiteration residual was one full order of magnitude lower than the estimated temporal error[24,30] for the x-momentum and turbulent kinetic energy residuals. The maximum number of subiterations per time step was set to 40; this limit was used in cases where the turbulent kinetic energy residual was not decreasing quickly enough. A non-dimensional time step of 0.0004 (dimensionally, 2.5×10^{-6} sec) was specified for the one nozzle configuration, yielding just over 200 time steps per cycle in the force history. The time step was reduced by half to 1.25×10^{-6} sec for the three and four nozzle configurations. The case for the three

nozzle configuration converged to steady-state for both this time step and a time step of 6.25×10^{-7} sec. The axial force oscillation frequency was determined from this information for the one nozzle and four nozzle configurations.

Kleb, et al.[4] examined the aspects of physical modeling related to tunnel wall interference and the complicated sting and high pressure feedline structure aft of the model (see Fig. 2). Comparing the effect of modeling the tunnel walls as inviscid walls or neglecting the walls altogether, they found the effect on the pressure distribution to be significant for cases at an angle of attack of 12° and negligible for cases at zero angle of attack. The tunnel walls in this investigation were modeled as inviscid walls, as all cases here were for zero angle of attack. As visible in Fig. 2, the geometry of the support hardware aft of the model is complex and protrudes into large areas of the subsonic wake flow. Kleb, et al.[4] explored the effect of modeling or not modeling the sting hardware at multiple angles of attack for both the one nozzle and three nozzle configurations. They found sting effects to be limited to the base and the three furthest aft pressure ports on the model and concluded that, for pressure comparisons over the rest of the body, modeling the complex sting hardware is not necessary at this time. Accordingly, the outer mold line of the model used here consists of only the forebody, aftbody, and aft face.

B. Conditions and Run Summary

A baseline zero nozzle case and a "jet-on" case for each nozzle configuration were considered, all at zero angle of attack. Additional cases at angle of attack remain as future work due to the computationally intensive nature of SRP problems.

The conditions for these cases were selected based on the apparent steadiness of the flowfield and lack of wall interaction in the high-speed schlieren video. The SRP flowfield was most steady (i.e. exhibited primarily local unsteadiness) at higher thrust coefficients, and the wall interactions were less significant at higher freestream Mach numbers. With these considerations, the flow conditions selected correspond to M_∞ = 4.6 (Re_∞/ft = 1.5×10^6) and C_T = 2.

Table 1. Conditions summary for CFD comparison cases.

Zero nozzle configuration – Run 283

Freestream conditions					Nozzle conditions			
M_∞	$p_{0,\infty}$ (psi)	p_∞ (psi)	$T_{0,\infty}$ (K)	T_∞ (K)	$p_{0,j}$ (psi)	$T_{0,j}$ (K)	$\dot{m}$ (lb_m/s)	$C_{T,total}$
4.600	25.40	0.0775	338.9	64.77	–	–	–	–

One nozzle configuration – Run 165

Freestream conditions					Nozzle conditions			
M_∞	$p_{0,\infty}$ (psi)	p_∞ (psi)	$T_{0,\infty}$ (K)	T_∞ (K)	$p_{0,j}$ (psi)	$T_{0,j}$ (K)	$\dot{m}$ (lb_m/s)	$C_{T,total}$
4.600	25.40	0.078	338.7	64.73	598.9	345.6	0.620	1.968

Three nozzle configuration – Run 247

Freestream conditions					Nozzle conditions (per nozzle)			
M_∞	$p_{0,\infty}$ (psi)	p_∞ (psi)	$T_{0,\infty}$ (K)	T_∞ (K)	$p_{0,j}$ (psi)	$T_{0,j}$ (K)	$\dot{m}$ (lb_m/s)	$C_{T,total}$
4.600	25.40	0.078	339.1	64.81	201.2	346.4	0.272	1.919

Four nozzle configuration – Run 307

Freestream conditions					Nozzle conditions (per nozzle)			
M_∞	$p_{0,\infty}$ (psi)	p_∞ (psi)	$T_{0,\infty}$ (K)	T_∞ (K)	$p_{0,j}$ (psi)	$T_{0,j}$ (K)	$\dot{m}$ (lb_m/s)	$C_{T,total}$
4.600	25.40	0.078	338.7	64.74	151.9	343.5	0.273	1.923

V. Grid Refinement Study

A grid refinement study was completed using the one nozzle configuration (and associated Run 165 conditions) to understand the sensitivity of solutions to grid spacing and also to assess the spatial accuracy

of the numerical scheme applied (FUN3D is spatially second-order accurate). The study was also used to establish grid generation guidelines for the other three configurations. A baseline grid was generated with a medium-fine grid density, and three coarser grids were then generated from this baseline grid. While the unstructured grid generation process used cannot be scaled linearly, the background grid spacing and surface grid spacing were scaled to approximate grid densities of 75%, 50%, and 25% (as compared to the grid density of the baseline grid). The approximate spacings for the baseline grid are given in Table 2, non-dimensionalized by model diameter.

Following the recommendations of Kleb, et al.,[4] two error quantities were tracked: C_L and a derived error quantity based on C_D for the finest grid. Run 165 is a single nozzle case at zero angle of attack; accordingly, C_L should be zero. The second error quantity was computed as the difference between C_D of the finest grid (Grid A, 55.2M nodes) and C_D of the current grid. Both error quantities are plotted against a function of the number of nodes, $N^{-2/3}$, in Fig. 4. Table 3 summarizes the grid characteristics and error quantities for each case. The axial force oscillation frequency was observed to increase with increasing grid resolution, with the frequency from the two finest grids agreeing well with the frequencies determined by several other CFD codes for this case.[4,21]

FUN3D is spatially second-order accurate for smooth flows, and in Fig. 4, the dashed line indicates a unity slope for second-order accuracy. Figure 4(a) shows the lift error to be noisy but tracking reasonably well with the second-order trend line. Computational resources limited the number of cases able to be run, and with the noisy behavior of the error quantities, results for the drag-based error quantity (Fig. 4(b)) were inconclusive. The increased resolution of additional flow features and sources of unsteadiness with increasing grid resolution also likely contributed to the noisy behaviors observed. Kleb et al.[4] were able to run this same case for a family of 7 grids and observed noisy behavior in the same error quantities. They also observed an approach toward a transition to first-order spatial accuracy with increasing grid refinement, an expected result for non-smooth flows.

Table 2. Approximate baseline grid spacing.

	Far field	Interaction region	Nozzle exit	Shoulder
Grid spacing (in model diameters)	0.32	0.0055 to 0.0063	0.0031	0.0047

Table 3. Summary of grid refinement study.

	Approximate grid density (as % of baseline grid density)	No. of surface nodes	Total no. of grid nodes	Oscillation frequency (kHz)	$C_{L,f}$	$C_{D,finest}$ - C_D
Grid A	100%	2.839M	55.21M	2.036	6.46×10^{-4}	–
Grid B	75%	2.338M	29.15M	1.858	3.08×10^{-4}	0.0012
Grid C	50%	1.791M	17.19M	1.761	1.18×10^{-4}	0.0011
Grid D	25%	1.140M	10.90M	1.673	2.67×10^{-4}	0.0008

Figure 5 illustrates the effect of grid resolution more qualitatively using Mach contours in the interaction region of the flowfield. As grid resolution increased, flow features sharpened as expected, particularly the shocks, shear layers, and jet boundaries. Additionally, the Mach number distribution within the jet changed with grid resolution. The Mach number in the jet increased more rapidly and to a higher value away from the nozzle exit with increasing grid resolution. The protuberance along the centerline was due to the use of a conical shell volume source; a full-volume conical source was used for all other cases in this investigation.

The desired grid resolution for the cases of interest in this investigation was severely limited by available computational resources. To this end, grids for the zero, three, and four nozzle configurations were constructed to have approximately 65% of the baseline grid density. As mentioned, the conical shell volume source in the jet region was replaced with a full cone.

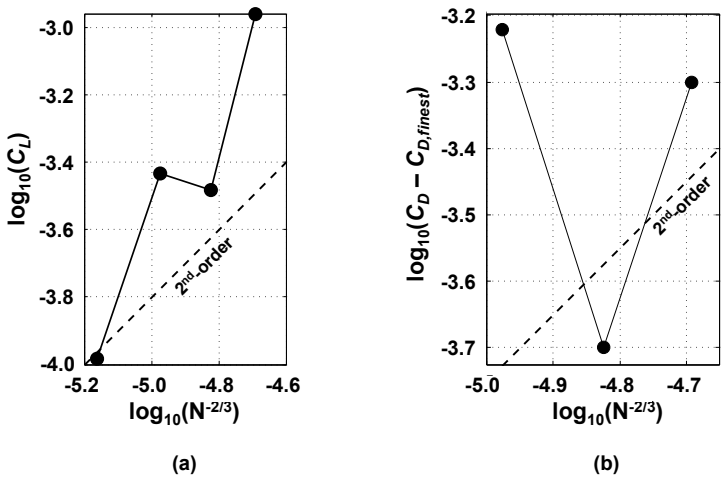

Figure 4. Error quantities related to lift and drag as functions of grid resolution.

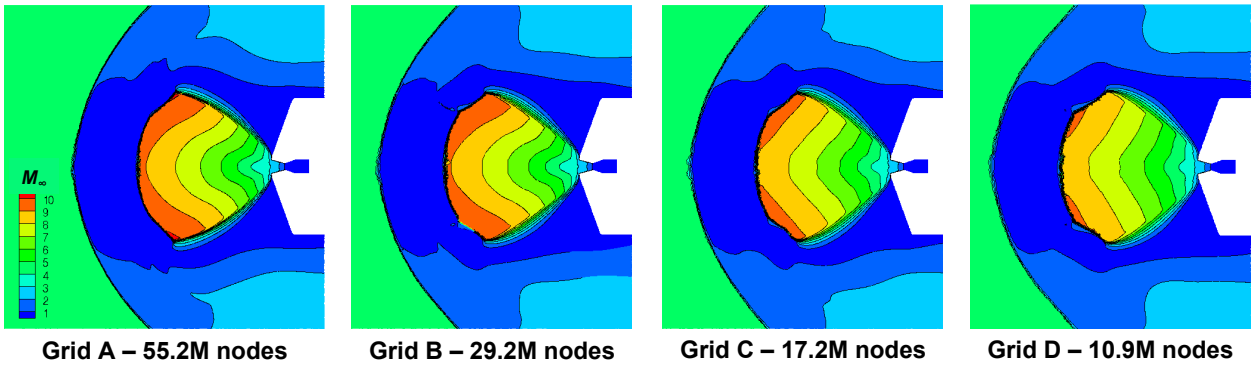

Figure 5. Mach contours illustrating the effect of grid resolution on SRP flowfield structure.

VI. Results

The results in this section have been compared directly with pressure data from the wind tunnel test described in Section III. Uncertainties on the experimental data are not yet available; as such, no error bars are given for the experimental data points during comparison, and no statements about the quality of the experimental data have been made. Computational flowfield schlieren images, C_p contours, and C_p as a function of location on the body are given for each of the four configurations. The one, three, and four nozzle results were all generated using a time-accurate approach; time-averaged results are presented. During the experiment, the model position was not adjusted to correct for an approximately 1° tunnel flow angle, potentially explaining some of the asymmetry in the pressure data with the model at zero angle of attack.[4] All figures for this section have been placed together at the end of the section.

A. Zero Nozzle Configuration

The case run for the zero nozzle configuration was the baseline case in this investigation. Figure 6 shows the forebody C_p contours and computational flowfield schlieren for the zero nozzle configuration. Figures 7(a) and 7(b) compare FUN3D results with experimental data for pressure coefficient. The C_p contours and flowfield features in Fig. 6 are as expected for a 70-deg sphere-cone forebody at zero angle of attack: axisymmetric with the highest pressure at the nose and decreasing outboard toward the shoulder and the position of the bow shock close to the body. The FUN3D results agree well with the experimental data on both the forebody and the aftbody for the four radial locations compared.

B. One Nozzle Configuration

Figure 8 shows the progression of forebody C_p contours and computational flowfield schlieren images through one complete cycle in the axial force history. All of the prominent flow features are visible; the bow shock is displaced upstream by a highly under-expanded jet (Mach disk, reflected shock intersection, barrel shock). The progression illustrates the unsteady nature of the flowfield, with the dominant oscillation frequency being that of the shedding of the annular vortex in the stagnation region. This shedding is communicated through the subsonic shear layer and recirculation regions over the forebody to the nozzle exit and back up along the supersonic shear layer along the jet boundary. The shedding of this annular vortex follows a change in the expansion at the nozzle exit due to a change in the local static pressure arising from the previous disturbance traveling through the flowfield. This feedback mechanism has been shown to be a predominantly inviscid phenomena and is discussed in greater detail by Bakhtian, et al.[32] As discussed in Section V, the dominant oscillation frequency was found to depend strongly on grid resolution, and for the medium grid applied here, the oscillation frequency of the axial force for the one nozzle configuration with C_T = 1.968 is 1.86 kHz. The time histories for the total axial force coefficient, normal force coefficient, and pitching moment coefficient across 0.002 seconds are given in Fig. 9. Note that the contribution of the jet flow is included in these results.

Figure 10(a) and 10(b) compare FUN3D results with the experimental data. On the forebody, the pressure taps show the pressure coefficient abruptly dropped outboard of the nozzle exit (r/r_m = 0.1 corresponds to the nozzle exit) and then remained nearly constant over much of the forebody, with the exception of rising slightly toward the shoulder. This pressure drop is substantial as compared to the zero nozzle configuration at the same conditions and is the direct result of the shielding of the body by the jet structure. The contact surface is the new effective freestream flow obstruction for supersonic retropropulsion flowfields. The pressure taps on the aftbody show some asymmetry, though this may be due to the aforementioned 1° tunnel flow angle for all of the zero angle of attack cases discussed here.

On the forebody, FUN3D captured the pressure drop outboard of the nozzle, including the rise toward the shoulder. The FUN3D results along three separate rays show good symmetry in the time-averaged C_p distributions, though FUN3D appears to be slightly under-predicting C_p across the entire forebody as compared to the raw experimental data. The same trends are seen in the FUN3D aftbody C_p distributions. It is interesting to note that a slight pressure rise toward the shoulder was seen here in both the experimental data and the FUN3D results. Prior work[6,19] has shown a slight pressure rise toward the shoulder for CFD results based on the configuration and conditions from Jarvinen and Adams[15] (sphere-cone forebody with a single, central nozzle and $C_T \approx 2$). However, the experimental data given for the Jarvinen and Adams[15] cases did not show the same pressure rise.

C. Three Nozzle Configuration

The case for the three nozzle configuration, though run as time-accurate, converged to steady-state, even after the time step was reduced from 2.5×10^{-6} seconds to 6.25×10^{-7} seconds. The results below are for the steady-state converged case. Additional work remains to identify a target frequency for this case, as the high-speed schlieren video taken during the experiment for this case, even at zero angle of attack, showed the flowfield to be highly unsteady.

Figure 11 shows the forebody C_p contours and computational flowfield schlieren images for the three nozzle configuration with a total C_T of 1.919. The forebody C_p contours are symmetric, as is consistent with the convergence of the solution to steady-state. The pressure in between the nozzles drops from the nose to approximately the 2/3 r location on the forebody before rising again toward the shoulder. The flowfield schlieren with surface C_p contours illustrates the impact of the jet interaction structure on the surface pressure distribution. Visible in the schlieren are two of the three jets, each with distinct highly under-expanded jet structure. In these FUN3D results, the interaction between the jets inboard of the nozzle exits is seen to maintain significant pressure between the nose and the nozzle exits at the half-radius. Also visible is a recompression shock off of the body shoulder.

The experimental data for the forebody show higher pressures at the nose, with a gradual decrease in pressure toward the shoulder for the 0° and 240° rays. Recalling the pressure tap layout shown in Fig. 3, the 0° and 240° rays run through nozzles, and the 180° and 300° rays run through the midpoint between two nozzles. The experimental data show a rise in pressure toward the shoulder for the 180° and 300° rays, behavior similar to though more pronounced than that observed for the one nozzle configuration.

FUN3D is over-predicting the pressure at the nose as compared to the raw experimental data, a result observed previously in CFD solutions for SRP flowfields with multiple nozzles.[6,16,19,20] Along the 0° and 240° rays, FUN3D follows the trend of the experimental data, though with values slightly lower than the experimental values outboard between the nozzle exit and the shoulder. However, the pressure rise observed experimentally along the rays between the nozzles beginning near r/r_m = 0.4 appears to be only minimally captured by FUN3D. FUN3D predicts higher pressures at the nose and lower pressures in between nozzles than were observed in the raw experimental data, indicating that the interaction between the individual jets may not be fully captured. The flowfield structure implies that the FUN3D solutions do not have sufficient inboard jet expansion at these conditions. While this result seems to be consistent across several CFD codes that have been applied to SRP configurations of concentrically arranged nozzles, the direct cause remains an open question. It has been suggested that one cause may be related to the tendency of two equation turbulence models to over-predict the jet spreading rate as a result of compressibility effects. The SST turbulence model applied here does not include any compressibility correction. The aftbody C_p distributions agree more favorably than the forebody C_p distributions as the pressure drops past the shoulder and remains approximately constant at a level near that of the freestream static pressure.

D. Four Nozzle Configuration

Figure 13 shows the forebody C_p contours and computational flowfield schlieren images for the four nozzle configuration. Similar to the three nozzle configuration, the case for the four nozzle configuration was also run initially as time-accurate and converged to steady-state. Reduction of the time step from 2.5 $\times$ 10^{-6} sec to 1.25 $\times$ 10^{-6} sec resulted in capturing the expected unsteady behavior. The addition of the center nozzle eliminated all significant pressure inboard of the concentric nozzles and evened out the pressure distribution over much of the forebody as compared to the three nozzle configuration. The center nozzle also reduced the unsteadiness in the intersecting shear layers and jet boundaries observed experimentally for the three nozzle configuration. In comparing the computational flowfield schlieren images in Fig. 13, the bow shock resembles that of the baseline zero nozzle configuration (Fig. 6) but for a flow obstruction with a larger area. The displacement of the bow shock by the individual jets seen for the three nozzle configuration (Fig. 11) is no longer seen with the addition of a center jet. At this condition ($C_{T,total} \approx 2$, α = 0°), the four nozzle configuration was observed on the high speed schlieren video during the wind tunnel test to be substantially more steady than the three nozzle configuration.

The time histories for the total axial force coefficient, normal force coefficient, and pitching moment coefficient across 0.002 seconds are given in Fig. 14. Note that the contribution of the jet flow is included in these results. Figure 15 shows the experimental C_p data and FUN3D results for the four nozzle configuration. As expected from the flowfield, the forebody pressure data are nearly constant at approximately the freestream static pressure. The pressure rise along the midpoint between nozzles seen in the three nozzle configuration forebody data is no longer present with the addition of the center nozzle. Additionally, the experimental data for the four nozzle configuration is much more symmetric on both the forebody and aftbody than in the other three cases, including the baseline.

The FUN3D results compare well on both the forebody and the aftbody, though there is a decrease in pressure just before and just after the nozzle exits that is not seen in the experimental data. C_p is noisy on the forebody as a result of needing to average the pressures over a long time period, but the overall trends in C_p given by FUN3D compare favorably with the given experimental data. The FUN3D predictions for the four nozzle configuration are significantly better than for the three nozzle configuration and at least as good as for the one nozzle configuration. The slight under-prediction by FUN3D across all three SRP configurations (as compared to the raw experimental data) is potentially due to the turbulence modeling applied; this is an area of further investigation by the CFD community working with supersonic retropropulsion flowfields.[4] Completion of the uncertainty analysis for the experimental data is needed to fully assess the performance of the specific RANS CFD approach applied here.

A comparison of all four cases is given in Table 4. The single nozzle finest grid case from the grid resolution study has been included to illustrate potential differences arising from grid resolution. All force coefficients are for the forebody only. The one nozzle and four nozzle cases use time-averaged quantities; the zero nozzle and three nozzle cases use steady-state values.

Table 4. Summary of aerodynamic force results for all four configurations.

	$C_{D,f}$	$C_{L,f}$	$C_{D,f}$ Oscillation frequency (Hz)	Steps / cycle
Zero nozzle	1.482	6.50×10^{-4}	–	–
One nozzle	0.019	6.46×10^{-4}	1.86	217
One nozzle (finest)	0.018	3.08×10^{-4}	2.04	198
Three nozzle	0.016	-7.95×10^{-4}	–	–
Four nozzle	0.019	1.17×10^{-4}	2.58	313

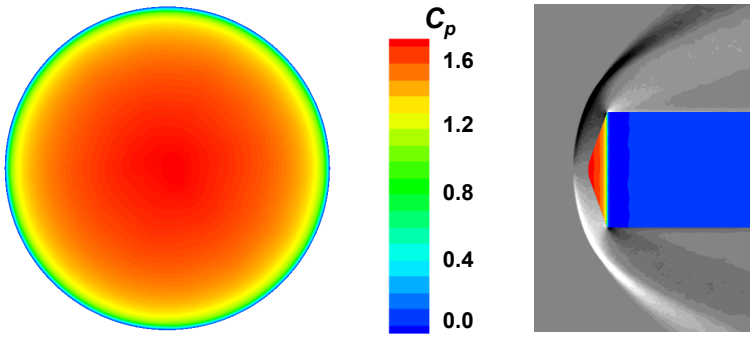

Figure 6. Forebody C_p contours and computational flowfield schlieren for the zero nozzle configuration.

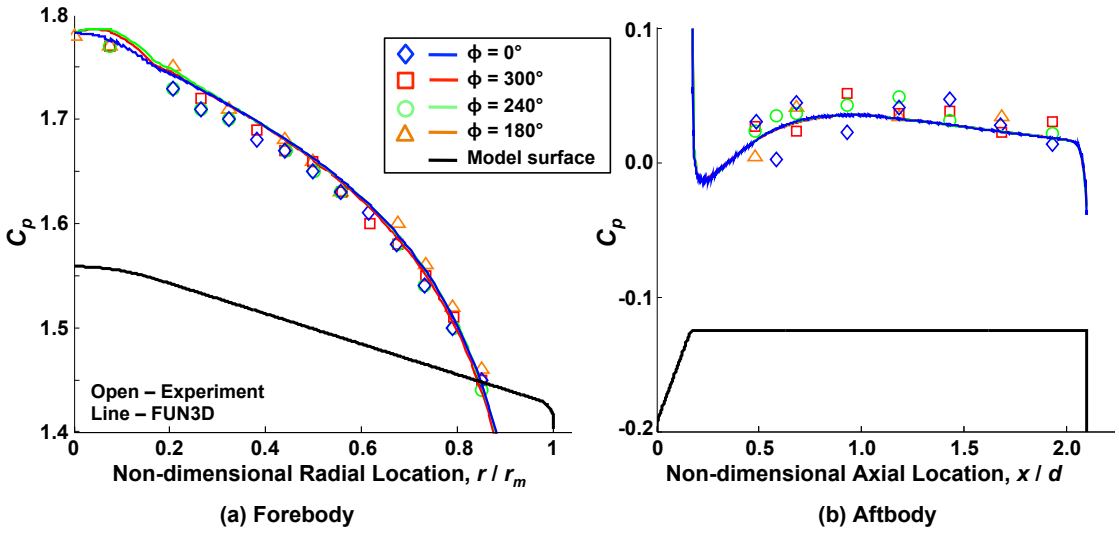

Figure 7. Comparison of C_p for the zero nozzle configuration.

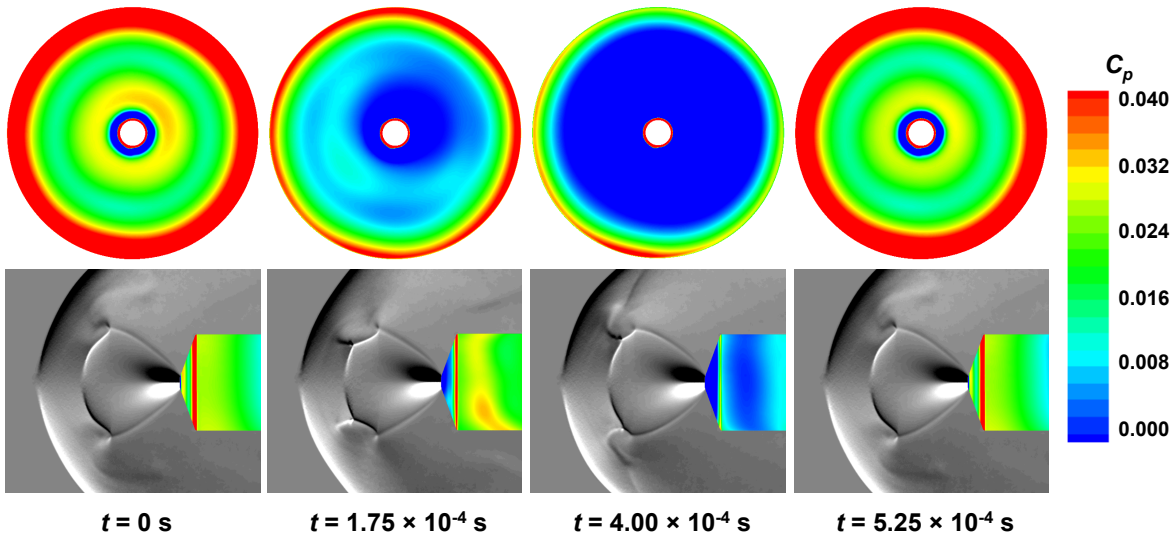

Figure 8. Forebody C_p contours and computational flowfield schlieren for the one nozzle configuration through one complete drag force oscillation cycle, depicting the shedding of the annular vortex.

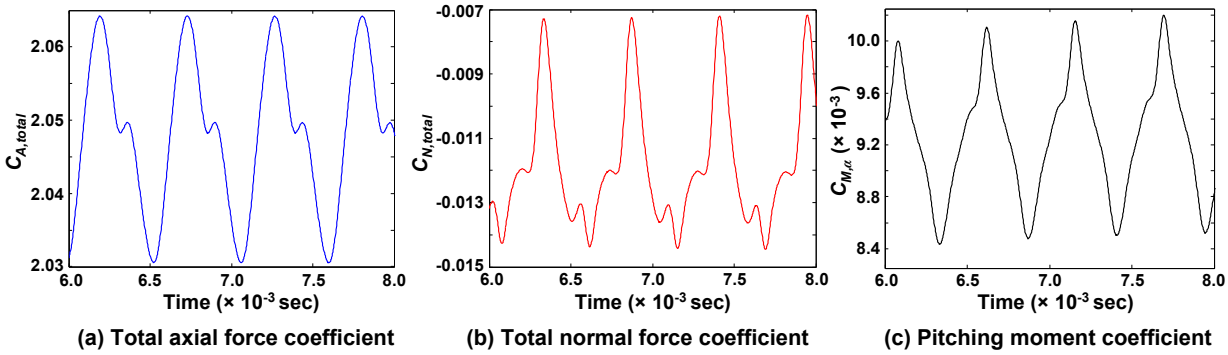

Figure 9. Portion of the axial force, normal force, and pitching moment coefficient time histories for the one nozzle configuration.

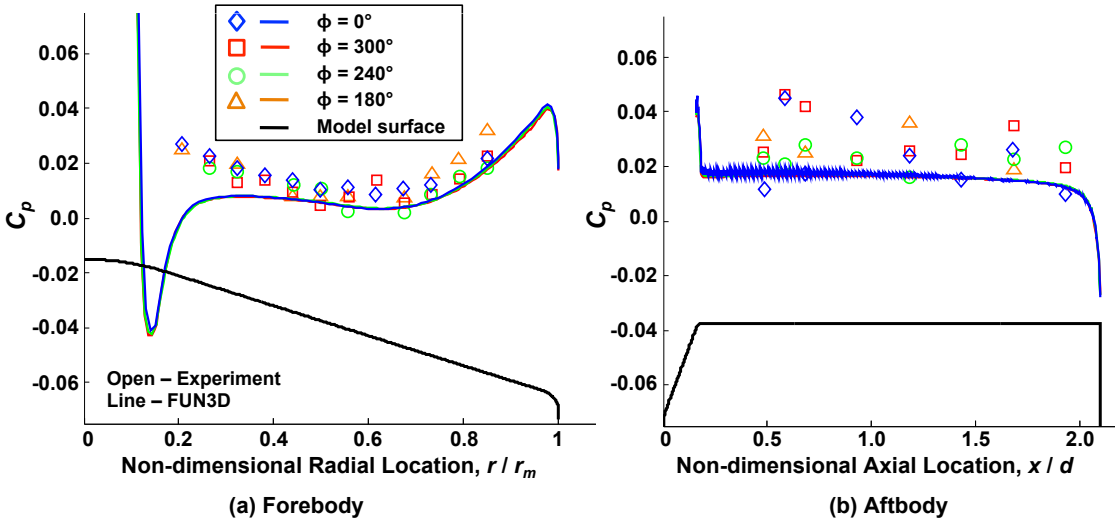

Figure 10. Comparison of C_p for the one nozzle configuration.

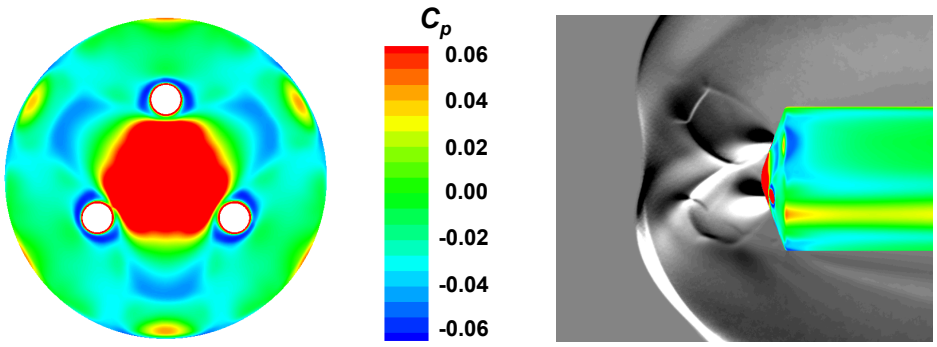

Figure 11. Forebody C_p contours and computational flowfield schlieren for the three nozzle configuration (converged to steady-state).

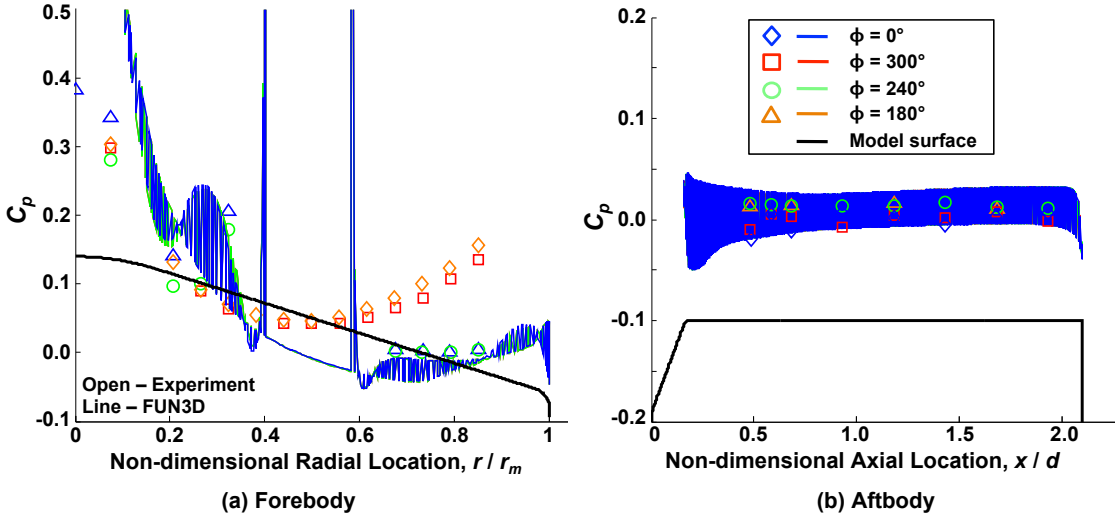

Figure 12. Comparison of C_p for the three nozzle configuration.

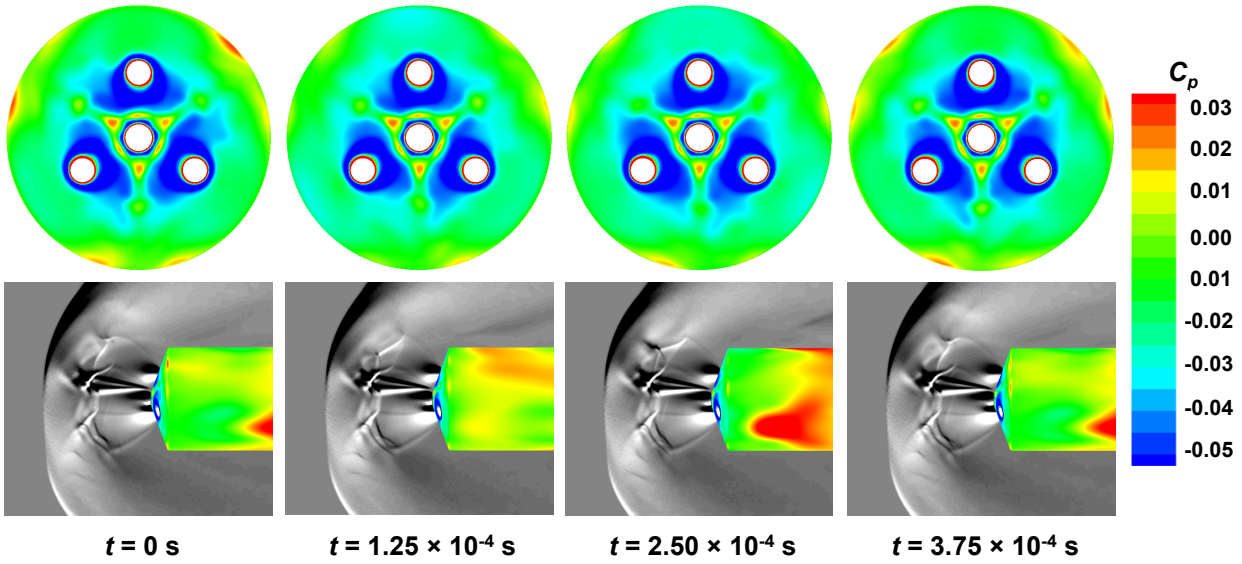

Figure 13. Forebody C_p contours and computational flowfield schlieren for the four nozzle configuration through one complete drag force oscillation cycle, depicting similar vortex shedding behavior as the one nozzle configuration.

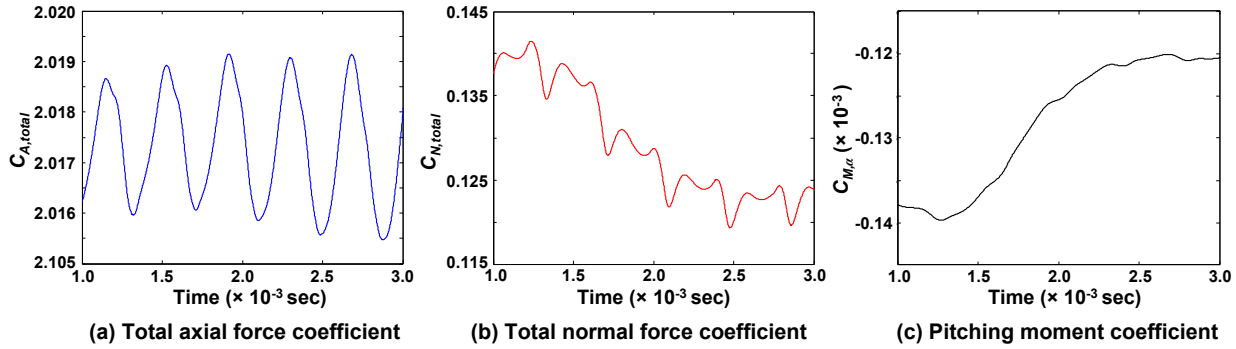

Figure 14. Portion of the axial force, normal force, and pitching moment coefficient time histories for the four nozzle configuration.

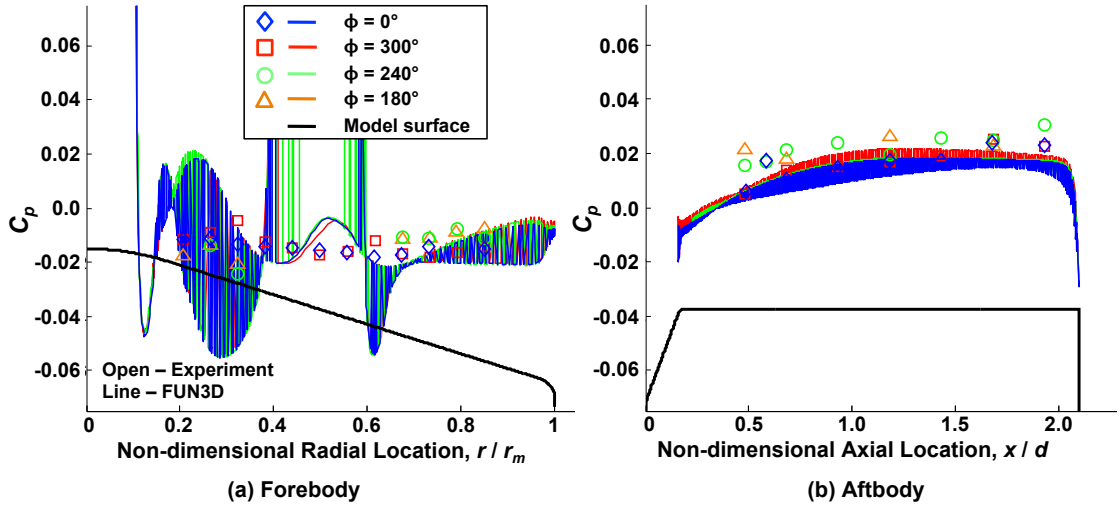

Figure 15. Comparison of C_p for the four nozzle configuration.

VII. Conclusions

Supersonic retropropulsion is a candidate decelerator technology for increasing landed mass capability and potentially enabling human exploration at Mars. Validated computational fluid dynamics methods will be required to develop aerodynamic models for vehicle concepts utilizing supersonic retropropulsion. This work supports SRP development efforts in computational analysis by applying a RANS CFD approach to multiple nozzle configurations and conditions from a recent wind tunnel test. This test was designed explicitly to provide data for CFD validation of SRP flowfield simulations, and comparisons of CFD solutions with static pressure data have been made.

Four configurations were explored (all at zero angle of attack): zero nozzles, one nozzle at the center, three nozzles equally spaced at the half-radius, and four nozzles from the combination of the one and three nozzle configurations. The RANS approach applied here performed well in predicting the C_p distributions on the forebody and aftbody for the one nozzle and four nozzle configurations. For the one nozzle case, the dominant frequency was found to be that of the shedding of the annular vortex in the stagnation region and was consistent with the frequency determined from the original experiment. For the four nozzle case, the behavior was similar to that of the one nozzle case, with a frequency determined for the shedding of an annular vortex off of a coalesced jet structure. The approach performed less well in predicting the C_p distributions for the three nozzle configuration. The three nozzle case converged to steady-state, even with a reduced time step, and the RANS approach was unable to fully predict the forebody C_p distribution, over-predicting pressure inboard of the nozzles and under-predicting pressure outboard between the individual nozzles. All cases showed good qualitative agreement with the flowfield structures and flowfield behaviors observed in the original experiment. Work remains to investigate cases at angle of attack for each configuration and to re-evaluate the performance of this RANS approach once the uncertainty analysis and full data reduction efforts have been completed for the original experiment.

Appendix

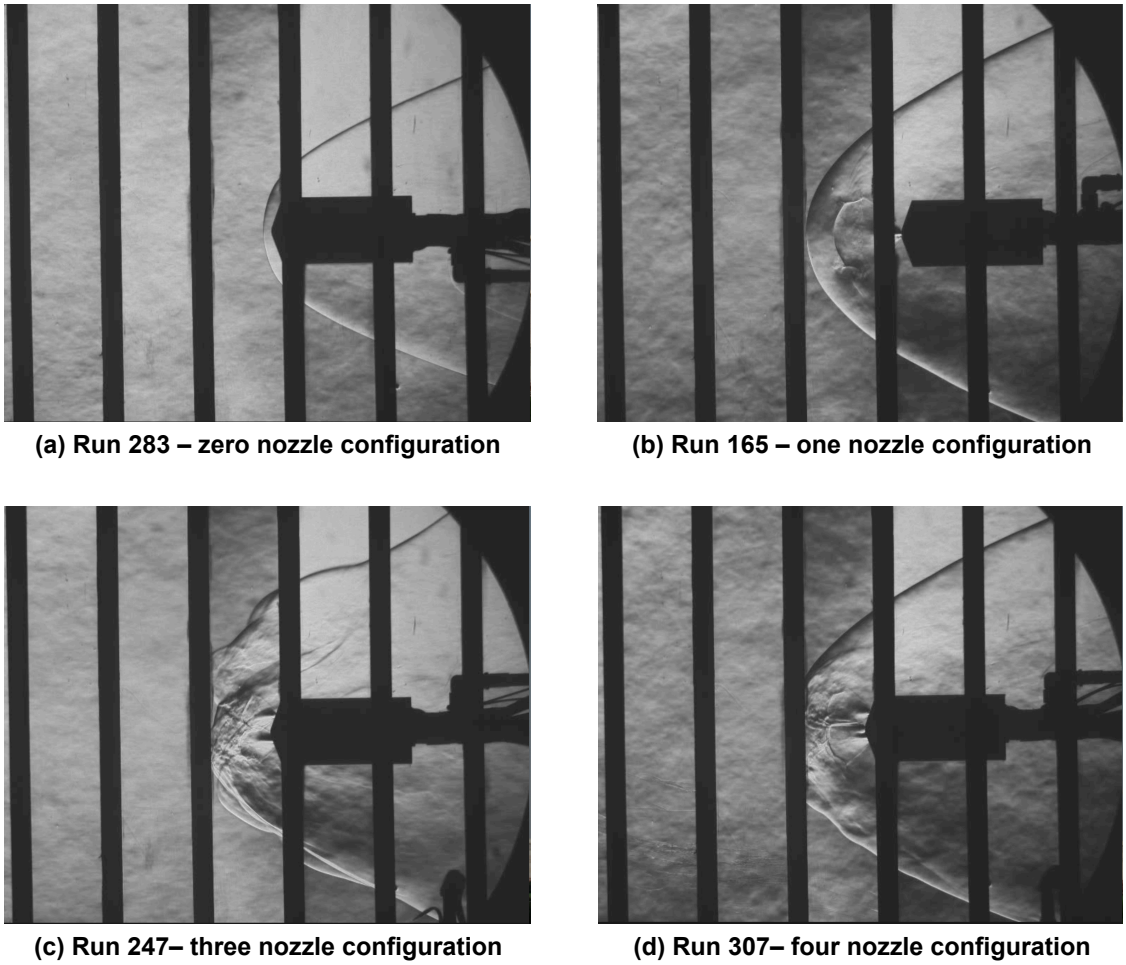

(a) Run 283 – zero nozzle configuration

(b) Run 165 – one nozzle configuration

(c) Run 247– three nozzle configuration

(d) Run 307– four nozzle configuration

Figure 16. Examples of schlieren images taken during testing for each case.[21]

Acknowledgments

The authors would like to thank the following individuals for their assistance and support of this work: Bil Kleb (NASA LaRC), Jan-Renee Carlson (NASA LaRC), Bill Jones (NASA LaRC), Guy Schauerhamer (NASA JSC), Scott Berry (NASA LaRC), Matt Rhode (NASA LaRC), and Karl Edquist (NASA LaRC). The authors would also like to acknowledge the support of this work by the NASA Exploration Technology Development and Demonstration Program, Supersonic Retropropulsion element.

References

[1]Braun, R. D. and Manning, R. M., "Mars Exploration Entry, Descent, and Landing Challenges," *Journal of Spacecraft and Rockets*, Vol. 44, No. 2, March-April 2007, pp. 310–323.

[2]Zang, T. A. and Tahmasebi, F., "Entry, Descent and Landing Systems Analysis Study: Phase 1 Report," TM 2010-216720, NASA, July 2010.

[3]Korzun, A. M., Braun, R. D., and Cruz, J. R., "Survey of Supersonic Retropropulsion Technology for Mars Entry, Descent, and Landing," *Journal of Spacecraft and Rockets*, Vol. 46, No. 5, September-October 2009, pp. 929–937.

[4]Kleb, W. L., Carlson, J.-R., Buning, P. G., Berry, S. A., Rhode, M. N., Edquist, K. T., Schauerhamer, D. G., Trumble, K. A., and Sozer, E., "Toward Supersonic Retropropulsion CFD Validation," No. AIAA 2011-3490, AIAA Thermophysics Conference, June 2011.

[5]Trumble, K. A., Schauerhamer, D. G., Kleb, W. L., Carlson, J.-R., and Edquist, K. T., "Analysis of Navier-Stokes Codes Applied to Supersonic Retro-Propulsion Wind Tunnel Test," No. 1471, IEEE Aerospace Conference, March 2011.

[6]Korzun, A. M., Cordell, C. E., and Braun, R. D., "Comparison of Inviscid and Viscous Aerodynamic Predictions of Supersonic Retropropulsion Flowfields," No. 2010-5048, AIAA, June 2010.

[7]Berry, S. A., Laws, C. T., Kleb, W. L., Rhode, M. N., Spells, C., McCrea, A. C., Trumble, K. A., Schauerhamer, D. G., and Oberkampf, W. L., "Supersonic Retro-Propulsion Experimental Design for Computational Fluid Dynamics Model Validation," No. 1499, IEEE Aerospace Conference, March 2011.

[8]Finley, P. J., "The Flow of a Jet from a Body Opposing a Supersonic Free Stream," *Journal of Fluid Mechanics*, Vol. 26, No. 2, October 1966, pp. 337–368.

[9]Pindzola, M., "Jet Simulation in Ground Test Facilities," AGARDograph 79, November 1963.

[10]Wilkes, J. A., Glass, C. E., Danehy, P. M., and Nowak, R. J., "Fluorescence imaging of underexpanded jets and comparison with CFD," No. 2006-910, AIAA, January 2006.

[11]Orth, R. C., Schetz, J. A., and Billig, F. S., "The Interaction and Penetration of Gaseous Jets in Supersonic Flow," CR 1386, NASA, July 1969.

[12]Salas, M. D., "The Numerical Calculation of Inviscid Plume Flow Fields," No. 1974-523, AIAA, June 1974.

[13]Korzun, A. M. and Braun, R. D., "Performance Characterization of Supersonic Retropropulsion for High-Mass Mars Systems," *Journal of Spacecraft and Rockets*, Vol. 47, No. 5, September-October 2010, pp. 836–848.

[14]Daso, E. O., Pritchett, V. E., Wang, T. S., Ota, D. K., Blankson, I. M., and Auslender, A. H., "Dynamics of Shock Dispersion and Interactions in Supersonic Freestream with Counterflowing Jets," *AIAA Journal*, Vol. 47, No. 6, June 2009, pp. 1313–1326.

[15]Jarvinen, P. O. and Adams, R. H., "The Aerodynamic Characteristics of Large Angled Cones with Retrorockets," CR NAS 7-576, NASA, February 1970.

[16]Bakhtian, N. M. and Aftosmis, M. J., "Parametric Study of Peripheral Nozzle Configurations for Supersonic Retropropulsion," *Journal of Spacecraft and Rockets*, Vol. 47, No. 6, November-December 2010, pp. 935–950.

[17]Chang, C.-L., Venkatachari, B. S., and Cheng, G. C., "Effect of Counterflow Jet on a Supersonic Reentry Capsule," No. 2006-4776, AIAA, July 2006.

[18]Cheng, G. C., Neroorkar, K. D., Chen, Y. S., Wang, T. S., and Daso, E. O., "Numerical Study of Flow Augmented Thermal Management for Entry and Re-Entry Environments," No. 2007-4560, AIAA, June 2007.

[19]Trumble, K. A., Schauerhamer, D. G., Kleb, W. L., Carlson, J.-R., Buning, P. G., Edquist, K. T., and Barnhardt, M. D., "An Initial Assessment of Navier-Stokes Codes Applied to Supersonic Retro-Propulsion," No. 2010-5047, AIAA, June 2010.

[20]Cordell, C. E., Clark, I. G., and Braun, R. D., "CFD Verification of Supersonic Retropropulsion for a Central and Peripheral Configuration," No. 1190, IEEE Aerospace Conference, March 2011.

[21]Berry, S. A., Rhode, M. N., Edquist, K. T., and Player, C. J., "Supersonic Retropropulsion Experimental Results," No. AIAA 2011-3489, AIAA Thermophysics Conference, June 2011.

[22]Anderson, W. K. and Bonhaus, D. L., "An Implicit Upwind Algorithm for Computing Turbulent Flows on Unstructured Grids," *Computers and Fluids*, Vol. 23, No. 1, January 1994, pp. 1–21.

[23]Anderson, W. K., Rausch, R. D., and Bonhaus, D. L., "Implicit/Multigrid Algorithm for Incompressible Turbulent Flows on Unstructured Grids," *Journal of Computational Physics*, Vol. 128, No. 2, October 1996, pp. 391–408.

[24]NASA Langley Research Center, http://fun3d.larc.nasa.gov/, *FUN3D Manual*, August 2010.

[25]Edwards, J. R., "A Low-Diffusion Flux-Splitting Scheme for Navier-Stokes Calculations," *Computers and Fluids*, Vol. 26, No. 6, July 1997, pp. 653–659.

[26]Albada, G. D. V., Leer, B. V., and Roberts, W. W., "A Comparative Study of Computational Methods in Cosmic Gas Dynamics," *Astronomy and Astrophysics*, Vol. 108, No. 1, April 1982, pp. 76–84.

[27]Menter, F. R., "Two-Equation Eddy-Viscosity Turbulence Models for Engineering Applications," *AIAA Journal*, Vol. 32, No. 8, August 1994, pp. 1598–1605.

[28]Jones, W. T., *GridEx Manual*, NASA Langley Research Center, December 2001.

[29]Garriz, J. A., *VGRID 3.2 Reference Documents*, ViGYAN, Inc., preliminary draft ed., September 1998.

[30]American Institute of Aeronautics and Astronautics, *Editorial Policy Statement on Numerical and Experimental Accuracy*, October 2010.

[31]Vatsa, V. N., Carpenter, M. H., and Lockard, D. P., "Re-evaluation of an Optimized Second Order Backward Difference (BDF2OPT) Scheme for Unsteady Flow Applications," No. 2010-0122, AIAA, January 2010.

[32]Bakhtian, N. M. and Aftosmis, M. J., "Analysis of Inviscid Simulations for the Study of Supersonic Retropropulsion," No. AIAA 2011-3194, AIAA Applied Aerodynamics Conference, June 2011.